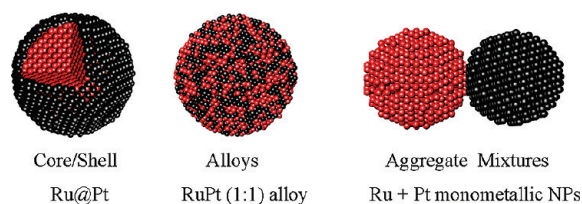# Structural and Architectural Evaluation of Bimetallic Nanoparticles: A Case Study of Pt−Ru Core−Shell and Alloy Nanoparticles

Selim Alayoglu,[†] Peter Zavalij,[†] Bryan Eichhorn,[†,]* Qi Wang,[‡] Anatoly I. Frenkel,[‡] and Peter Chupas[§]

[†]Department of Chemistry and Biochemistry, University of Maryland, College Park, Maryland 20742, [‡]Department of Physics, Yeshiva University, New York, New York 10016, and [§]X-ray Science Division, Argonne National Laboratory, Argonne, Illinois 60439

Monometallic and bimetallic nanoparticles (NPs) are key components in many catalytic, optical, and magnetic devices. The ability to control the composition, shape,[1−3] and architecture[4−6] of multicomponent NP systems is of increasing importance in tailoring the resulting properties. Synthetic approaches to NP synthesis have been evolving over the last 100 years, but most structural/compositional information is gleaned from TEM and XRD analysis.[7−10] These methods are quite satisfactory for large NPs (>10 nm), but obtaining similar information for smaller, catalytically relevant particles of less than 5 nm is more challenging.[11−15] The vast majority of bimetallic NP catalysts are prepared by impregnation/deposition methods that often give well-dispersed, highly active systems, but the details of structure and local composition are difficult to ascertain and often remain ill-defined.[16,17] For example, the structure and oxidation states of Pt and Ru in active PtRu fuel cell electrocatalysts remain a contentious topic.[18]

We have recently shown that bimetallic particles of the same size, shape, and composition show significant differences in activity when configured into different architectures, such as alloy, core−shell, or monometallic mixtures (see drawing).[5] In particular, the core−shell structure has emerged as an attractive catalytic component due to the ability to tune the activity of the shell metal through interactions with the core.[4,5,19−23] However, rational design and control of the particle's activity requires precise synthetic methodology and full knowledge of structure/composition.
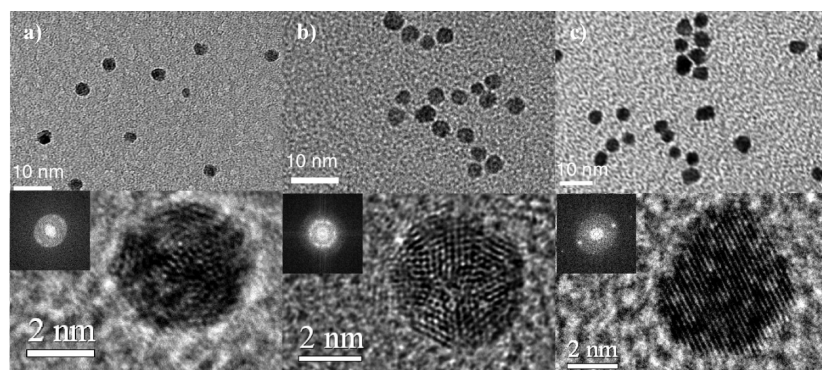
The structure, composition, and architecture of bimetallic nanoparticles are defined by many parameters. For example, the nanoparticle shape (*e.g.*, cuboctahedral *versus* truncated octahedral) is a distinct structural characteristic, in addition to the crystal structure (*i.e.*, fcc *vs* hcp).[24−27] In addition, bimetallic nanoparticles with the same composition, shape, and crystal structure can have different architectures

ABSTRACT A comprehensive structural/architectural evaluation of the PtRu (1:1) alloy and Ru@Pt core−shell nanoparticles (NPs) provides spatially resolved structural information on sub-5 nm NPs. A combination of extended X-ray absorption fine structure (EXAFS), X-ray absorption near edge structure (XANES), pair distribution function (PDF) analyses, Debye function simulations of X-ray diffraction (XRD), and field emission transmission electron microscopy/energy dispersive spectroscopy (FE-TEM/EDS) analyses provides complementary information used to construct a detailed picture of the core/shell and alloy nanostructures. The 4.4 nm PtRu (1:1) alloys are crystalline homogeneous random alloys with little twinning in a typical face-centered cubic (fcc) cell. The Pt atoms are predominantly metallic, whereas the Ru atoms are partially oxidized and are presumably located on the NP surface. The 4.0 nm Ru@Pt NPs have highly distorted hcp Ru cores that are primarily in the metallic state but show little order beyond 8 Å. In contrast, the 1−2 monolayer thick Pt shells are relatively crystalline but are slightly distorted (compressed) relative to bulk fcc Pt. The homo- and heterometallic coordination numbers and bond lengths are equal to those predicted by the model cluster structure, showing that the Ru and Pt metals remain phase-separated in the core and shell components and that the interface between the core and shell is quite normal.

KEYWORDS: core−shell · nanoparticles · EXAFS · catalysts · structure−property relationships

Core/Shell
Ru@Pt

Alloys
RuPt (1:1) alloy

Aggregate Mixtures
Ru + Pt monometallic NPs

Figure 1. TEM images showing (top) general morphology and (bottom) high-resolution images of (a) a 3.0 nm Ru NP, (b) a 4.1 nm Ru@Pt NP, and (c) a 4.4 nm PtRu alloy NP. Insets show the FFTs of HR-TEM images.

(*i.e.*, spherical fcc PtRh alloys and core−shell NPs).[28] Recent studies have shown that shape, structure, composition,[29] and architecture[4,5,28] are extremely important parameters affecting catalytic activities of bimetallic nanostructured materials, and, as such, knowledge of these parameters is critical in understanding the underlying surface science and catalytic chemistry.

We report here a comprehensive architectural evaluation of the PtRu alloy and Ru@Pt core−shell NPs that provides spatially resolved structural information on sub-5 nm NPs. This comparative study illustrates how extended X-ray absorption fine structure (EXAFS), X-ray absorption near edge structure (XANES), pair distribution function (PDF) analyses, Debye function simulations of X-ray diffraction (XRD), and field emission transmission electron microscopy/energy dispersive spectroscopy (FE-TEM/EDS) analyses provide complementary information used to construct a detailed picture of the core−shell and alloy nanostructures. In particular, we can clearly differentiate NPs of the same size and show that core−shell structures comprise essentially metallic, crystallographically disordered Ru cores with thin, 1−2 monolayer Pt shells. Moreover, these shells are grown in a nonepitaxial, pseudomorphic fashion with only slight distortions from bulk Pt metal. EXAFS and XANES studies show a small but significant oxidation of Pt in Ru@Pt core−shell NPs, which is noticeably absent in the alloy and pure Pt particles. In contrast, the PtRu alloy NPs are homogeneous random alloys that show a higher degree of Ru oxidation relative to the Ru@Pt core−shell but a complete absence of Pt oxidation. These structural and spectroscopic signatures provide insight to the unique and unusual activities of the coreunique and unusual activities of the core−shell and alloy structures.

RESULTS

In our previous publication,[5] we described the synthesis, general characterization, and catalytic activity of Ru@Pt core−shell and PtRu alloy NPs. In particular, surface IR-CO probe experiments and catalytic activities were used to differentiate alloy from core−shell archi-

tectures. Here we use direct methods to evaluate distortions of the surface structure, details of alloy formation, and the nature of the interfacial interactions between core and shell components of the Ru@Pt particles. In the Discussion, we compare and contrast the core−shell and alloy NPs to illustrate how the various techniques can differentiate the two types of architectures.

Composition and Architecture by Scanning Transmission Electron Microscopy. The high-resolution TEM images of the Ru NPs (Figure 1a) show them to be roughly spherical in shape with ill-defined lattice fringes. Some faceting is also observed, but well-defined facets are not easily identifiable. The Ru@Pt NPs show well-defined lattice fringes that are associated with the crystalline 1−2 monolayer (ML) thick Pt shells (Figure 1b). The fast Fourier transform (FFT) analyses of the particle images show highly faceted fcc Pt NPs. In contrast, the HR-TEM image of the PtRu alloy (Figure 1c) shows 111 faceted fcc NPs with large, crystalline domains.

Although the HR-TEM images of the alloy and core−shell particles appear very similar, the local composition and architecture (core−shell *vs* alloy) are easily distinguished using a 1.5 nm EDS probe in the STEM mode. Multiple single-particle EDS analyses of core−shell and alloy NPs from various syntheses confirmed that all particles are bimetallic in nature, and stray monometallic particles were not observed in any of the samples. STEM-EDS line scans recorded from 4.1 nm Ru@Pt NPs clearly show a bimodal Pt distribution that reaches a maximum at the edge of the particle (*i.e.*, the shell), whereas the Ru L line shows maximum Ru concentration at the center of the particle (Figure 2a). In addition, STEM-EDS point spectra acquired from different regions of a distinct Ru@Pt NP show the highest atomic % Pt at the edges with more atomic % Ru at the center (Supporting Information, Figure S1). In contrast, the PtRu alloy NPs show single Gaussian distributions of X-rays across the particle for both elements, as expected from the random arrangement of atoms on the surface and in the bulk of the particle (Figure 2b). STEM-EDS point spectra acquired from different regions of the same particle also reveal the random arrangement of Pt and Ru atoms across the particle (Supporting Information, Figure S2).
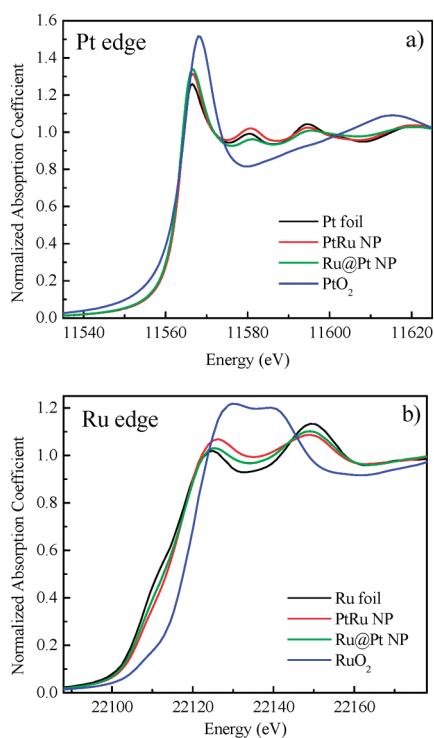
Extended X-ray Absorption Fine Structure (EXAFS) and X-ray Absorption Near Edge Structure (XANES) Studies. XANES and EXAFS data were collected for PtRu and Ru@Pt NPs to evaluate the electronic structure and the atomic configuration geometry in their local environment. Bulk Pt, Ru, RuO_2, and PtO_2 standards were also evaluated for comparison. The XANES data show predominantly metallic states of Ru and Pt in both the core−shell and alloy NP samples (Figure 3). However, the NP samples
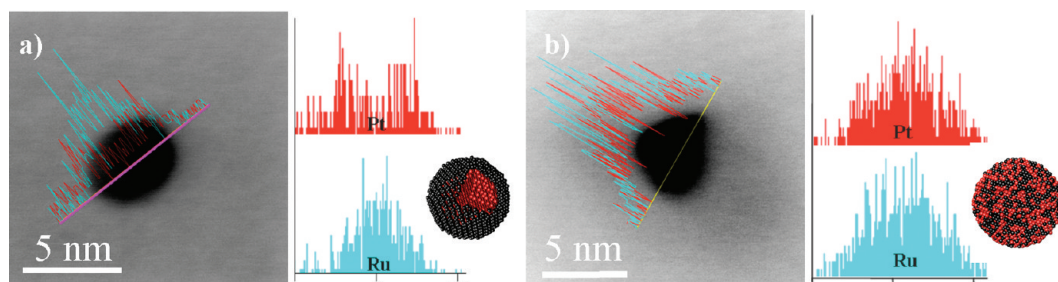
Figure 2. Representative STEM-EDS line spectra of (a) a 4.0 nm Ru@Pt NP and (b) a 4.4 nm PtRu (1:1) alloy nanoparticle. Relative atomic % composition values (vertical axis) of Pt (red) and Ru (blue) are plotted against the line scan probe position (horizontal axis) and are given next to the STEM images. A 1.5 nm probe was used to trace 10−15 nm scans across each particle. The particle centers are at ∼5 nm in (a) and ∼7 nm in (b).

consistently exhibit increasing white line intensities as well as shifts to higher energies relative to the bulk Pt and Ru, indicating some degree of oxidation. The Ru@Pt NPs show the highest Pt white line intensity (Figure 3a) of the two nanoparticle samples, indicating that the Pt was slightly more oxidized in the Ru@Pt core−shell NPs relative to the PtRu NP alloy and the Pt foil standard. Strong oxidation of Pt should be ruled out based on comparison with bulk Pt and PtO_2 (Figure 3a). The Ru in both NPs also exhibited some degree of oxidation, especially in the PtRu alloy structure, but both NP samples were much more akin to metallic Ru than RuO_2 (Figure 3b).

The raw, edge-step normalized and background-subtracted EXAFS data in k space and the corresponding Fourier transforms in r space at both Pt L_3 and Ru K edges are displayed in Supporting Information, Figure
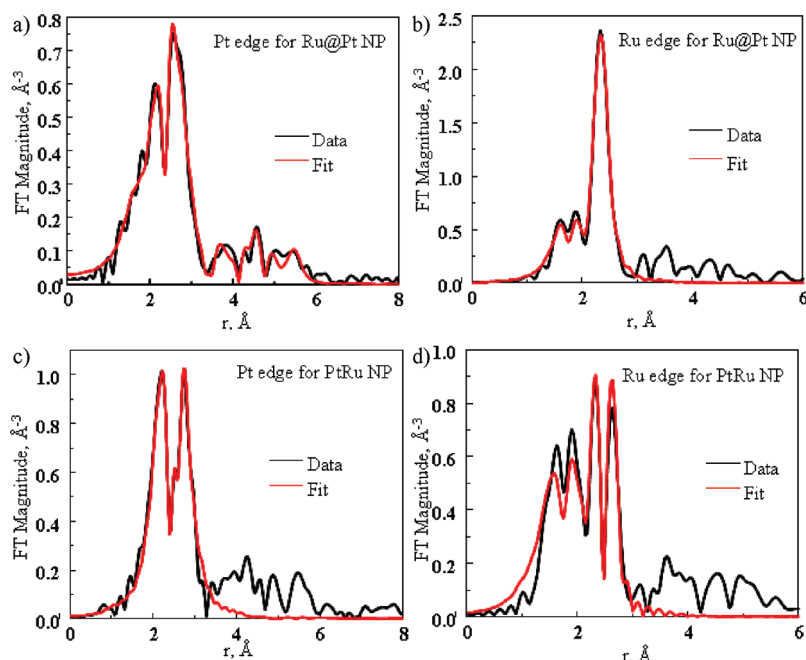
S3. The EXAFS oscillations in k space at each absorption edge are lower in amplitude compared to that in bulk Pt and Ru (Supporting Information, Figure S3a,b), which can be attributed to the finite size effect of nanoparticles. The EXAFS oscillations in the Ru@Pt core−shell NPs are in phase with bulk behavior at the Ru edge and are phase-shifted to slightly higher k values at the Pt edge, which is consistent with the presence of Ru metal in the core and a somewhat distorted Pt shell. In contrast, k space oscillations for the PtRu alloy NPs are significantly phase-shifted from their respective metal standards at each edge, which is consistent with the more random mixing of Pt and Ru within the nanoparticles. In addition to having the lower amplitude of the first nearest neighbor (1NN) peaks at both Pt and Ru edges, which can be attributed to the size truncation effect expected in the nanoparticles, their r space data, in particular, for the Ru K edge, demonstrate the signs of alloying (in PtRu alloy NP) or segregation (in Ru@Pt NP) as well (Supporting Information, Figure S3c,d). Comparison of the EXAFS signals in standard Pt and Ru oxides and those in the nanoparticle samples confirms the observation made by XANES that Pt and Ru bonding with oxygen is insignificant, if at all present.

EXAFS data and theoretical fits for the Pt L_3 edge and the Ru K edge of the Ru@Pt and PtRu NPs are shown in Figure 4. EXAFS data analysis was carried out by simultaneously fitting both the Pt edge and Ru edge data while accurately accounting for homometallic (Pt−Pt and Ru−Ru) and heterometallic (Pt−Ru and Ru−Pt) interactions. The best-fit values of the 1NN structural parameters are summarized in Table 1.

Multiple-scattering contributions to the Pt edge data calculated from the fcc model of pure Pt were also included in the FEFF analysis of Ru@Pt NPs, such that data at higher r range could be fitted to extract structural parameters beyond the first coordination shell (Figure 4a). Good fit quality and physically meaningful values of the best-fit results validated the approximation used in the fit, that the Pt environment is Pt-rich in that sample. For the Ru edge data, the absence of such high-order contributions was taken as evidence of the poorly ordered core structure (Figure 4b). These EXAFS data show that the Ru cores of the

Figure 3. XANES spectra of (a) Ru@Pt core/shell NPs, PtRu alloy (1:1) NPs, Pt foil, and PtO_2 at the Pt L_3 edge and (b) Ru@Pt core/shell NPs, PtRu alloy (1:1) NPs, Ru and RuO_2 powders at the Ru K edge.

Figure 4. Fourier transform magnitudes of the FEFF6 theory (red) to the EXAFS data at (a) Pt L$_3$ edge and (b) Ru K edge for the Ru@Pt core/shell NPs, and at (c) Pt L$_3$ edge and (d) Ru K edge for the PtRu alloy (1:1) NPs.

Ru@Pt NPs are highly disordered with few discernible interactions beyond the first nearest neighbor peak. These findings are also entirely consistent with the XRD and TEM studies that show poorly crystalline Ru NP seeds prior to Pt coating.

Comparisons of the experimental EXAFS results with models of 4.0 nm Ru@Pt NPs show that the data

are most consistent with ~3.0 nm Ru cores covered with 1−2 ML Pt shells. Pt−Pt coordination numbers of the first through fourth coordination shells for the Ru@Pt core−shell nanoparticles were calculated from various 4.0 nm model NPs comprising fcc Pt shells on highly disordered Ru cores (see Experimental Methods for details). The 4.0 nm NP size was based on the results from the TEM analysis described in the previous section. The distributions of pairwise M−M separations for the core−shell and alloy NP models are shown in Figure 5. The Pt−Pt coordination numbers of the first through fourth coordination shells of the 4.0 nm Ru@Pt models with 1 and 2 ML shells are given in Supporting Information, Table S1, along with the experimentally observed values. Given the weak order in the core, Ru contributions were expected to be small and the Pt−Ru interactions were not included in the modeling. It should be noted that the experimental Pt data also show reasonable agreement with a monometallic 1.1 nm Pt cluster. However, monometallic particles or any particles of that size have not been observed in any of the TEM studies.

X-ray Diffraction. Powder X-ray diffraction profiles of the PtRu (1:1) alloy NPs reveal an fcc structure that is intermediate to bulk fcc Pt and the fcc equivalent of metallic hcp Ru. Rietveld refinement of the synchrotron diffraction data yields a cubic lattice parameter, $a = 3.8771(3)$ Å, and a refined Pt/Ru ratio of 49(1):51(1) (Figure 6c). The lattice constant is very close to the 3.873 cell expected from a Vegard's law extrapolation for a 50:50 random alloy.

In contrast, the XRD patterns of the Ru@Pt core−shell NPs are a superimposition of the two components: a poorly crystalline Ru core and a distorted but relatively crystalline Pt shell (Figure 6a).

Modeling of the PtRu (1:1) alloy and Ru@Pt core−shell structures was accomplished by using the Debye function subroutine in the DISCUS software package.[36] Simulation of the core−shell structure required the Ru@Pt model structures to be entered as 4.0 nm clusters packed into an artificial 4.0 nm lattice as described in the Experimental Methods. The PtRu (1:1) alloy NP was modeled for a 4.4 nm cluster with random distribution of Pt and Ru atoms. As a result, there are no symmetry requirements and the observed simulations represent the diffractions of the unconstrained model structures. The calculated and observed diffraction data for the core−shell and alloy NPs are shown in Figure 6. Weak diffraction artifacts are generated from the intercluster spacings of the artificial lattice and are marked by asterisks in Figure 6a,b. The calculated and observed XRD patterns for the PtRu (1:1) alloy (Figure

TABLE 1. Structure Parameters and Estimated Uncertainties (in parentheses) from EXAFS Analysis of the Ru@Pt Core/Shell and PtRu Alloy (1:1) NPs

samples	bulk Pt foil	PtRu NP	Ru@Pt NP	bulk Ru foil
N_{Pt-Pt}	12	6.8 (3)	7.2 (4)	
N_{Pt-O}			1.1 (4)	
N_{Pt-Ru}		2.8 (3)	0.3 (1)	
N_{Ru-Pt}		4.0 (6)	0.4 (3)	
N_{Ru-Ru}		4.2 (9)	7.5 (5)	12 (6 + 6)
N_{Ru-O}		1.1 (7)	0.5 (3)	
N_{Pt-M}		9.6 (5)	7.4 (6)	
N_{Ru-M}		8.1 (1.1)	7.9 (5)	
R_{Pt-Pt} (Å)	2.774(2)	2.739 (2)	2.743 (3)	
R_{Pt-O} (Å)			1.998 (15)	
R_{Pt-Ru} (Å)		2.716 (3)	2.690 (10)	
R_{Ru-Pt} (Å)		2.716 (3)	2.690 (10)	
R_{Ru-Ru} (Å)		2.688 (6)	2.665 (3)	2.648 (2)
				2.707 (2)
R_{Ru-O} (Å)		1.965 (22)	1.967 (15)	
σ^2_{Pt-Pt} (Å^2)	0.0050 (1)	0.0055 (2)	0.0076 (3)	
σ^2_{Pt-O} (Å^2)			0.0116 (46)	
σ^2_{Pt-Ru} (Å^2)		0.0049 (5)	0.0027 (14)	
σ^2_{Ru-Pt} (Å^2)		0.0049 (5)	0.0027 (14)	
σ^2_{Ru-Ru} (Å^2)		0.0067 (12)	0.0061 (4)	0.0032 (2)
σ^2_{Ru-O} (Å^2)		0.0028 (39)	0.0000 (18)	

6b) show that the Debye analyses of the cluster models are quite effective in simulating the diffraction data.

The calculated and observed X-ray diffraction patterns for the 4.0 nm Ru@Pt core−shell NPs with *ca.* 1−2 ML Pt shells are shown in Figure 6a. Simulations of the XRD data show that the observed diffraction patterns are dominated by Pt and are consistent with 1−2 ML shells. The best simulations were obtained with highly distorted Ru cores (relative to hcp metallic Ru) that contributed little to the overall diffraction intensity. The Ru cores were distorted through MMC simulations[36] to better simulate the amorphous structure revealed by our EXAFS, TEM, and XRD studies of the Ru NP seeds. Debye simulations of the diffraction from the Pt shell with-

	Experiment	Model (average)
Pt-Pt	7.2(4)	7.43
Pt-Ru	0.3(1)	0.67

	Experiment	Model
Ru-Pt	4.0(6)	5.2
Ru-Ru	4.2(9)	5.0

Figure 5. Plots of pair distributions predicted from model Ru@Pt core−shell structures with a 2.0 ML Pt shell (top) and PtRu (1:1) alloys (bottom). The table insets show the calculated and observed EXAFS-derived partial coordination numbers of the two NP architectures.

out a Ru core also provide a reasonable match to the experimental data (see Figure 6a). In total, the simulations are entirely consistent with the model structure comprising slightly distorted 1−2 ML Pt shells deposited on essentially amorphous Ru cores.

Atomic Pair Distribution Function Analysis. The Ru@Pt core−shell and PtRu alloy NPs as well as monometallic Ru NPs were analyzed using atomic pair distribution function (PDF) analysis. The evaluation of diffraction data in terms of the total reduced structure factor, *F*(*Q*), and its Fourier transformed equivalent *G*(*r*), known as the atomic PDF, are well-documented techniques for probing the structures of small metallic NPs.[39] This technique is particularly powerful for assessing the 3-D structure of essentially amorphous nanomaterials with minimal long-range order. An excellent overview of the theory and application of PDF analysis on Ru NPs has been described by Petkov *et al.*[40]

Distorted model clusters as well as periodic phases were used for PDF simulations. The Ru and PtRu (1:1) alloy NP model clusters were constructed from periodic structures of hcp Ru and an fcc PtRu alloy that were truncated to give spherical particles with the experimentally observed mean particle size (3.0 nm Ru NPs and 4.4 nm PtRu alloy NPs). The Ru@Pt core−shell models were constructed by superimposing fcc Pt shells (1 or 2 MLs) on the Ru cores as described in the Experimental Methods. The Ru cores were randomly distorted by using MMC simulations, in accord with previous studies,[40] to provide better fits to the data. Drawings
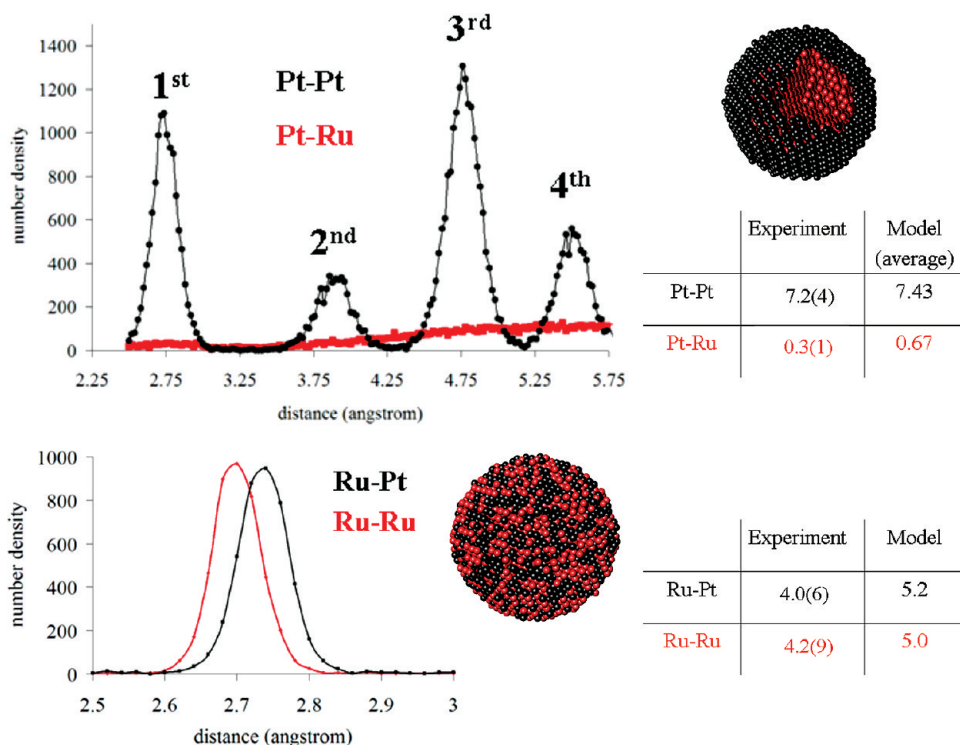
of the model clusters are shown in the insets of Figure 5.

Experimental PDFs of monometallic Ru, bimetallic PtRu (1:1) alloy, and Ru@Pt NPs are shown in Figure 7. Visual inspection of the three patterns shows that each has a different degree of long-range order and interatomic distances. The PtRu alloy NPs show long-range order that persists beyond 20 Å (Figure 7). The Ru@Pt core−shell NPs also show pair correlations out to 20 Å but with M−M separations different than those of the alloy. In contrast, 3.0 nm Ru particles show order extending over only a few atoms with virtually no pair contributions beyond 8 Å.

PDFs of monometallic Ru and bimetallic PtRu NPs were refined using PDFGUI software.[43] The initial fits of the PtRu (1:1) alloy data were performed using a simple periodic fcc model in which Pt and Ru were randomly substituted on the same metal site, and the particle size was spherically truncated at 4.4 nm (Figure 8a). The PDF refined lattice parameter (*a* = 3.879(1) Å) and site occupancies for Ru and Pt (0.52(1) and 0.48(1), respectively) are in excellent agreement with the Rietveld refinement of the XRD data (see Figure 6c). While the PDF refinement of the Ru data using a nondistorted periodic model yielded reasonable lattice parameters, the quality of the fit was poor—especially beyond *r* > 5 Å. The high degree of disorder in the Ru lattice is believed to be largely responsible for the poor fit (Supporting Information, Figure S4).
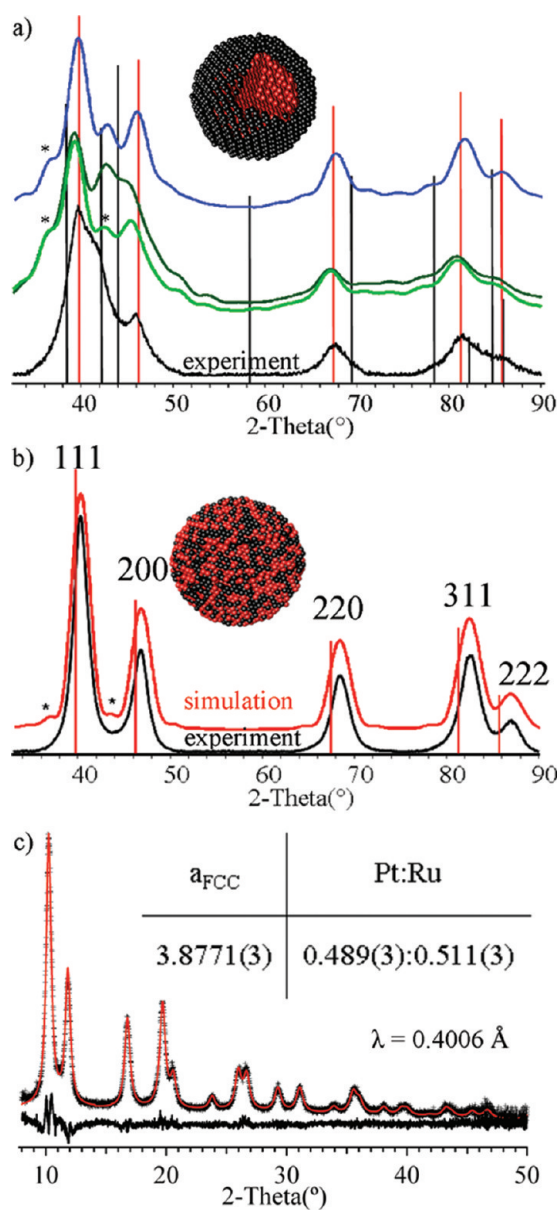
Figure 6. (a) XRD data showing Debye simulations of diffraction from a 4.0 nm Ru@Pt model cluster with a 1 ML Pt shell (top, blue), a Ru@Pt model cluster with a 2 ML Pt shell (middle, dark green), a 2 ML Pt shell alone (middle, light green), and the experimental diffraction data (bottom, black). The red and black stick patterns are the diffraction positions for bulk Pt and Ru metals, respectively. Asterisks denote diffraction artifacts arising from the periodicity of the artificial 5.0 nm lattice. The Ru cores are distorted from the ideal hcp structure by way of multi-energy Monte Carlo (MMC) transformations (see Experimental Methods). (b) Debye simulation (red pattern) of diffraction from 4.4 nm PtRu (1:1) random alloy cluster packed in a 5.0 nm lattice. The experimental data (black pattern) is shown below. The red stick patterns represent diffraction positions for bulk Pt metal. The Miller indices for the fcc reflections are shown. (c) Rietveld refinement of fcc PtRu random alloy (space group $Fm3m$) from synchrotron data showing experimental (black crosses), calculated (red line), and difference (black line, bottom) profiles. The refined parameters are given in the inset.

Although alloy and pure metals can easily be fit with periodic models, more sophisticated structures, such as the core−shell, can only be simulated and require cluster models. Because PDF simulation software requires crystallographic input (*i.e.*, period structures), we again constructed artificial lattices containing model NPs. Figure 8 shows the refinement of the PtRu alloy NP data using the "standard" periodic input described above (Figure 8a) and the simulations using the cluster model in the artificial cell (Figure 8b). The cluster model cell introduces an anomalous background above the average pair correlations due to the interparticle contacts imposed by the artificial cell;[44] however, the peak positions and intensities are in excellent agreement with the experimental data. Importantly, the comparison shows that the cluster models can provide excellent simulations of the pair distributions.

Simulations of the Ru@Pt PDF data were calculated using three different cluster models: an idealized Ru@Pt core−shell cluster, a two-phase simulation in which Ru cores and Pt shells were independent contributors, and a Pt shell-only model (Figure 9). All three simulations give reasonable peak positions and intensities at low *r*, but the differences between the simulated and experimental pair distributions are clearly discernible at high *r*. First, the Pt shell-only model simulation gives a very reasonable agreement with the experimental PDF, which suggests that most of the ordered pair correlations reside in the Pt shell. Second, the idealized Ru@Pt cluster model (with an ordered Ru core) gives the poorest agreement, presumably due to the overweighting of Ru interactions in the simulation. This problem is most apparent at *r* values >10 Å where the Ru core has no discernible pair correlations (see Figure 7). Finally, the best simulation was obtained with a separated core and shell model in which the poorly ordered Ru core was down-weighted relative to the Pt shell to better simulate a poorly crystalline core/crystalline shell structure (Figure 9, bottom). The resulting scale factors for the core and shell components in this refinement were 10:1 (Pt/Ru), indicating that the Ru cores had a negligible contribution to the total scattering of the particles.

DISCUSSION

The structural studies described here provide clear pictures of two types of NP architectures having the same composition and size. While XRD and TEM-EDS studies provide general information that differentiates the core−shell from the alloy NP types, EXAFS and PDF analyses provide detailed structural information regarding core and shell interfaces, local bonding environments (bond distances and coordination numbers), and total structural analysis on small, catalytically relevant NPs. Importantly, the data show that core−shell and alloy NPs are distinct architectures that can be unequivocally differentiated using the techniques described herein. Each architecture is described individually below.

PtRu(1:1) Alloy NPs. The experiments described above reveal that the PtRu (1:1) alloy NPs are homogeneous random alloys with large crystalline domains and rela-
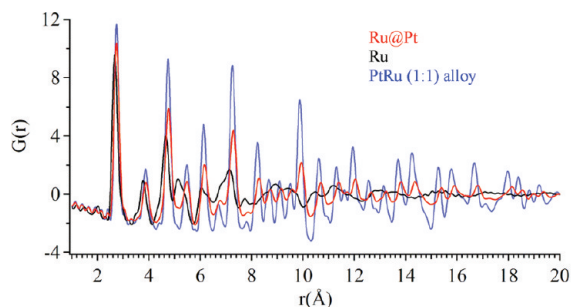
Figure 7. (a) Experimental PDFs of monometallic Ru (black), PtRu (1:1) alloy (blue), and Ru@Pt core/shell (red) nanoparticles.
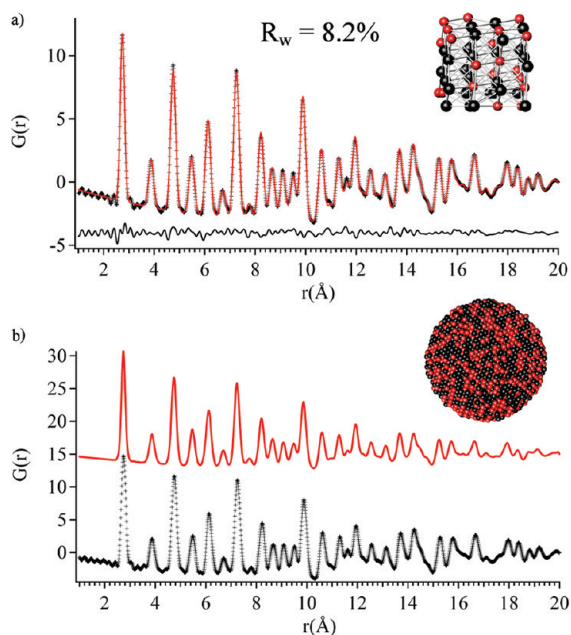

Figure 8. (a) PDF refinements of the PtRu (1:1) alloy NPs using the spherically truncated periodic model. The experimental data are shown by markers and the fits by solid lines. The difference between experiment and fit is presented below the plot. (b) Simulation of the PtRu alloy PDF (in red) using 4.4 nm alloy clusters packed in an artificial unit cell. The experimental PDF is shown in black.

tively long-range order throughout the 4.4 nm particle. The STEM-EDS experiments show that all of the NPs are bimetallic, and the line scans (Figure 2) illustrate that the Pt and Ru atoms are equally distributed throughout the particles (*i.e.*, a homogeneous random alloy). The XRD and PDF studies show that the alloy has the expected prototypical fcc structure with a lattice constant ($a = 3.971(3)$ Å) indicative of a random alloy with a 1:1 mixture of Pt and Ru. In addition, the refined Pt and Ru occupancies from the XRD (51:49 Pt/Ru) and PDF (52:48 Pt/Ru) studies both showed a 1:1 mixture of the elements, which is consistent with the 1:1 ratio of precursors used in the synthesis of the particles. As evidenced from EXAFS data in Table 1, the PtRu alloy has relatively high heterometallic coordination numbers, N, indicating a high degree of atomic mixing ($N_{Pt-Ru} = 2.8 \pm 0.3$ and $N_{Ru-Pt} = 4.0 \pm 0.6$). Such re-

sults are expected if the PtRu NP system has a random mixing of Pt and Ru at the atomic level.[41]

Heterometallic coordination numbers are related to the bulk composition:[36,37] $X_{Pt}/X_{Ru} = N_{Ru-Pt}/N_{Pt-Ru}$, where X is the molar fraction of each element in a binary compound, where the coordination number values are taken from EXAFS analysis (Table 1). This relationship holds regardless of the degree of short-range order (SRO) in the binary compound or an alloy. The calculated X_{Pt}/X_{Ru} value of 1.4 ± 0.3 for the PtRu alloy NPs (using the experimentally measured coordination numbers, Table 1) is close to the 1:1 ratio obtained independently by single-particle STEM-EDS, XPS measurements,[5] XRD and PDF refinements (see above), and the 1:1 ratio of precursors used in the particle synthesis. This result further validates the self-consistency of all experimental methods used in this work and adds credence to our definitive statements about the composition, structure, and architecture of the nanoparticles that emerged as a result of the combination of these techniques.

XANES experiments showed that both Pt and Ru were primarily in the metallic state in the PtRu alloy NPs, but the Ru showed a slight oxidation relative to the metallic Ru standard and the Ru@Pt core−shell NPs. Consistent with this finding, the EXAFS experiments showed measurable Ru−O contributions, whereas no measurable Pt−O contributions were detected. In addition, colloidal and surface IR experiments with CO probe molecules show both Pt and Ru on the surface of the alloy NP, but the surface Ru atoms are most susceptible to oxidation.
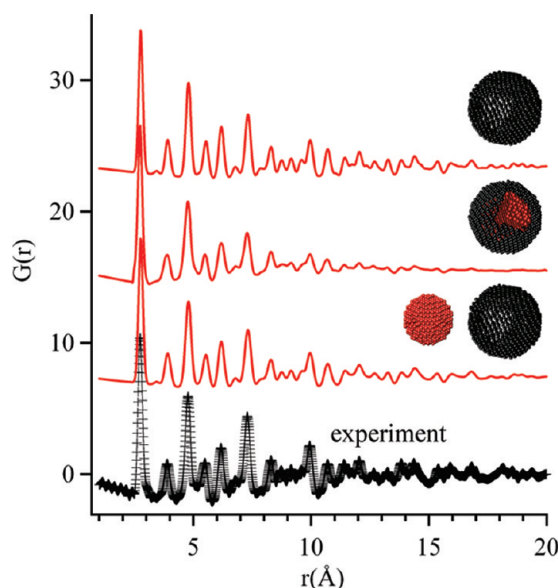
Figure 9. PDF simulations (in red) of the Ru@Pt core−shell NPs using ATOMS generated model clusters of (top) a 4.0 nm diameter 1356 atoms (2 ML) Pt skin, (middle) a single-phase 4.0 nm diameter Ru@Pt with 3.0 nm diameter Ru core and 2 ML thick Pt shell, and (bottom) a two-phase 4.0 nm diameter Pt skin and 3.0 nm diameter Ru. The experimental data are shown by black markers at the bottom.

Ru@Pt Core—Shell NPs. The cumulative data presented here reveal that the Ru@Pt core—shell NPs comprise very disordered, metallic Ru cores with relatively crystalline ~1.5 ML thick Pt shells. The STEM-EDS studies showed that all of the Ru@Pt particles are also bimetallic, but the distinctive bimodal distribution of the Pt in the particles (Figure 2) is indicative of a shell structure unlike those of an alloy or ordered intermetallic NP. The XANES experiments show that the Ru cores are primarily in the metallic state, but the XRD, PDF, and EXAFS data show that there is little order in the core structure. The Ru cores appear quite distorted from the structure of the bulk hcp metal and quite similar to the thiol-capped essentially amorphous Ru particles studies by Petkov *et al.*[40]

The EXAFS data provide valuable insight regarding the nature of the Pt shell as well as the Ru—Pt core—shell interface. In modeling the Pt EXAFS data, the best agreement with experiment is found when a mixture of the 1 and 2 ML Pt shells (*i.e.*, a 1.5 ML Pt shell) was employed in the model calculations (see Figure 5 and Supporting Information, Table S1). This finding is in excellent agreement with the 1.4 ML Pt shell predicted from the Schmid—Toshima[38] analysis of the particle size and composition. The Pt—Ru coordination numbers in the Ru@Pt NPs ($N_{Pt-Ru} = 0.3 \pm 0.1$ and $N_{Ru-Pt} = 0.4 \pm 0.3$) are small but measurable from fits of both the Pt and Ru experiments, indicating a limited number of heterometallic interactions between the Ru core and Pt shell.[41,42] Since the combination of TEM/EDS (Figure 2b) and XPS studies[5] indicates that the particles have relatively narrow size and composition distributions, the small Pt—Ru coordination numbers can be uniquely attributed to the interfacial interaction between the core and shell components and are very close to the $N_{Pt-Ru} = 0.67$ predicted from a pair distribution analysis of the model cluster (see Figure 5). Importantly, the EXAFS data show that the number of Pt—Ru interactions and their associated bond distances are very similar to that expected from the model structures and are very different from the PtRu alloy. These findings indicate that, despite the disorder in the Ru core, the Pt—Ru interface is quite normal and not significantly contaminated by oxide interlayers.

Interestingly, the Pt—Ru disorder parameters were obtained to be smaller for the Ru@Pt NPs compared to the PtRu (1:1) alloy NPs (Table 1). One possible explanation for this peculiar observation is a particular model of disorder in the Pt—Ru interface (between the Pt shell and Ru core). If there are two populations of Pt—Ru bonds at the interface, the strongly ordered and strongly disordered ones, EXAFS signal will be contributed by the relatively ordered pairs only (*i.e.*, ones with smaller disorder parameters, consistent with our results in Table 1), whereas the second population of bonds, the strongly disordered ones, will not contribute to EXAFS. Such bimodal distribution of Pt—Ru bonds may explain also the relatively low coordination numbers of Pt—Ru bonds obtained by EXAFS compared to the PDF analysis results (*vide supra*).

The XANES data show essentially metallic states for both Pt and Ru, but the Pt data for the Ru@Pt NPs show a higher degree of oxidation than the Pt foil reference or the PtRu alloy. Accordingly, we observed significant contributions from Pt—O interactions ($N_{Pt-O} = 1.1 \pm 0.4$) in the Ru@Pt NPs but no detectable Ru—O interactions, in sharp contrast to what was obtained for the alloy. These data collectively illustrate that the metals are in significantly different chemical environments in the core—shell *versus* alloy architectures. Moreover, the Ru core in the Ru@Pt structure is significantly less oxidized (more metallic) than either the PtRu alloy or the Ru NP seeds, again suggesting that the core—shell architecture has a significantly altered chemical environment relative to the alloy or monometallic NPs.

Finally, there are several interesting features associated with the Pt shell. We show through Debye function simulations and XRD experiments that relatively sharp X-ray diffraction peaks can be obtained from monolayer thick Pt shells. While the Pt diffraction positions and intensities are generally consistent with fcc Pt, non-uniform shifts in the profiles reveal distortions from the ideal fcc structure. In particular, the 200 reflection shifts to lower 2θ, while the reminder of the diffraction peaks are slightly shifted to higher 2θ values relative to metallic Pt. In addition, the EXAFS data show a slight compression of the Pt—Pt bonds relative to bulk Pt, which are consistent with DFT models and observed chemical activity.[45,46] The variations in peak positions signify distortions in the Pt structure that presumably arise from pseudomorphic growth of the Pt shell over the Ru core.[47−49]

In summary, we have documented and differentiated the structural details of Ru@Pt core—shell and PtRu alloy NPs of the same size and composition. The findings are based on a combination of TEM, EDS, EXAFS, XANES, PDF, and XRD studies that provide cumulative evidence for two different architectures. Importantly, the different architectures (core—shell *vs* alloy) impart marked differences in chemical activity. The Ru core in the Ru@Pt particle affects significant changes in the electronic and structural properties of the Pt shell that greatly influences the chemical activity of the system. The Pt—Pt and Pt—Ru interactions in the shell and core—shell interface, described in this study, provide insight into the origins of the anomalous behavior and provide excellent data for future model development. In both the PtRu alloy and Ru@Pt core—shell systems, the Ru is partially oxidized (~10−20%) but the Pt metal is only oxidized in the core—shell structure. The degree of oxidation of each metal varies with the particle treatment (H_2 *vs* O_2), but both the alloy and core—shell systems are primarily in the metallic

state in the conditions described here. In subsequent studies, we will show how the Ru@Pt core−shell NPs form surface alloy structures under oxidizing conditions and re-form core−shell structures under reducing conditions in a reversible fashion. These reversible changes in structure affect reversible changes in catalytic activity and provide a unique example of structure−activity relationships.

EXPERIMENTAL METHODS

Synthesis. The synthesis of Ru@Pt core−shell, PtRu alloys, and the monometallic Ru and Pt NPs has been described elsewhere.[5] The structural studies described below were all recorded from the same sample lots to facilitate direct comparisons.

TEM/STEM/EDS. A Jeol 2100F field emission transmission electron microscope (FE-TEM) equipped with an Inca energy dispersive spectrometer (EDS) was used for line and point spectra of nanoparticles. The FE-TEM was operated at 200 kV and in the scanning mode (STEM). FFT analysis was performed using Gatan Digital Micrograph software.

Powder X-ray Diffraction. A Bruker C2 Discover (Parallel Beam) general area diffraction detection (GADDS) system was used for powder diffraction measurements. A Bruker ACS Hi-Star detector was used in conjunction with a monochromatic Cu Kα radiation source biased at 40 kV and 40 mA. The diffraction patterns were acquired between 33 and 90° by integrating and merging four 2-D images covering a 14° range in 2θ collected with 10−15 min exposure times. The samples were oscillated in the xy plane to homogenize the diffracting grains.

Powder X-ray Diffraction Refinements. The general structure analysis system (GSAS) package[30] was employed to analyze and refine the synchrotron data of the 1:1 PtRu alloy NPs. The data were collected at the 11-BM-B beamline at the Advanced Photon Source of Argonne National Laboratory. A monochromatic 30 keV X-ray ($\lambda = 0.4$ Å) was used. For the alloy sample, a single-phase Rietveld refinement was conducted with Pt and Ru statistically mixed in an fcc structure.

Atomic Pair Distribution Function Analysis. Data suitable for PDF analysis were conducted at the 11-ID-B beamline at the Advanced Photon Source at Argonne National Laboratory using the rapid-acquisition PDF approach.[31,32] A general electric amorphous silicon detector was used in conjunction with high-energy X-rays (~59 keV). The data analysis was carried out using PDF-GETX2 and PDFGUI software packages. First, the intensity function, $I(Q)$, was calculated from the raw X-ray data using PDF-GETX2. The intensity function was corrected for the sample and instrument effects such as Compton scattering, Laue diffuse scattering, self-absorption, X-ray polarization, and weighting after background subtraction. The corrected intensity function was then used to calculate first the reduced structure function, $Q[S(Q) − 1]$, that was then Fourier transformed to the pair distribution function, $G(r)$. A model PtRu alloy cluster of Pt and Ru atoms was refined against the modified pair distribution functions for the alloy NPs. To simulate the PDF patterns from cluster models, Pt and Ru alloy NP cluster models were created using space group $Fm\bar{3}m$,[33] extended in space to a 4.4 nm diameter sphere using the PDFGUI software package, and refined as a periodic structure. The occupational probability of each atom site was initially set to 0.5 and temperature factors to 0.01 Å² for all Pt and Ru atoms, that is, a 1:1 alloy. Multiple variables including a low r cutoff factor and a Q damping factor were used in the simulation. The 4.0 nm core−shell clusters (see above section) consisting of a Ru core and shells of either 810 Pt atoms corresponding to 1 monolayer (1 ML) or 1356 Pt atoms (2 MLs) were independently simulated and compared to the pair distribution function for the core−shell NPs. Similarly, a randomly disordered 3055 atom (1:1) PtRu alloy cluster with a particle diameter of 4.4 nm was also simulated for comparison.

Extended X-ray Absorption Fine Structure (EXAFS) and X-ray Absorption Near Edge Structure (XANES) Studies. XAFS experiments were performed at beamline X-18B at the National Synchrotron Light Source (NSLS), Brookhaven National Laboratory, Upton, New York. The storage ring energy was 2.5 GeV, and the ring current was in the range of 110−300 mA. A double-crystal Si(111) monochromator was used to scan X-ray energy from −150 to 1800 eV relative to Ru K edge (22 117 eV) and from −150 to 1600 eV relative to Pt L₃ edge (11 564 eV). Each sample (~20 mg) was prepared by brushing the fine powder of the nanoparticles uniformly onto an adhesive tape, which was then folded several times for the absorption coefficient jump at the edge to be between 0.5 and 1. Transmission XAFS measurements were carried out with the pure Ru and Pt metals measured in reference mode simultaneously for X-ray energy calibration and data alignment. Data processing and analysis were performed using the IFEFFIT package.[34] EXAFS analysis was done model-independently, and the results were not biased in favor of any assumed model about the short-range order of elements in these samples. Specifically, multiple-edge (Pt L₃ and Ru K) analysis was employed by fitting theoretical FEFF6 calculations[35] to the experimental EXAFS data in r space.[15,17] The values of passive electron reduction factor, S_0^2, were obtained to be 0.87 and 0.83 for Pt and Ru, respectively, by fits to their corresponding standards (the error bars in these values were ± 0.03 and 0.05, respectively), and fixed in the analysis of the nanoparticles. The parameters describing electronic properties (*e.g.*, correction to the photoelectron energy origin) and local structural environment (coordination numbers N, bond length R, and their mean-squared relative derivation σ^2) around absorbing atoms were varied during fitting. In addition, the physically reasonable constraints between the fitting parameters, $R_{Pt−Ru} = R_{Ru−Pt}$ and $\sigma^2_{Pt−Ru} = \sigma^2_{Ru−Pt}$, for the first nearest neighbor (1NN) pairs were applied.

Modeling and Simulations. The models of the spherical core−shell nanoclusters were created by superimposing Pt shells of desired thicknesses over Ru cores of a desired size. Both core and shell components were generated separately using the ATOMS program. Powder diffraction patterns were simulated from the generated nanoclusters by using the Debye function in the DISCUS software package.[36] The model clusters were packed in artificial lattices with equilateral orthogonal axes (space group $P1$) and no imposed symmetry (except translational).

Two 4.0 nm core−shell clusters were generated using published Pt and Ru structural data for the bulk metals. One cluster consists of 1605 Ru atoms and 810 Pt atoms that correspond to a 3.5 nm Ru core and ~1 monolayer (ML) thick Pt shell. A second cluster consists of 922 Ru atoms and 1356 Pt atoms corresponding to a 3.0 nm Ru core and a ~2 ML thick Pt shell. The ATOMS-generated core−shell clusters were further distorted to register Ru and Pt atoms using the DISCUS multi-energy Monte Carlo function.[36] The atoms were moved in harmonic potentials, E_h, according to the equation

$$E_h = \sum_j \sum_n k_{n*}[d_{jn} - \gamma_{jn*}d_0]^2 \qquad (1)$$

where j is the site index, n is the neighbors around site j, d_{jn} is the distance between neighboring atoms, d_0 is the average distance, and γ_{jn} is the distortion. The sums were taken over all sites j and all neighbors n around site j.[36] The force constant k_n was fixed at an arbitrary value of 10 for all nearest neighbor pair interactions. The Hamiltonian was normalized using a restoring force constant k_0 (*i.e.*, a situation where $\gamma_{jn} = 0$), which was also arbitrarily fixed at 15 for all nearest neighbor pair interactions. EXAFS-measured metal−metal distances of $d_{Pt−Pt} = 2.743$ Å, $d_{Pt−Ru} = 2.690$ Å, and $d_{Ru−Ru} = 2.665$ Å were used. Pt atoms were allowed to shift isotropically by 0.005 Å and Ru atoms by 0.015 Å. Thermal factors (*i.e.*, Debye−Waller parameters) were also taken into account in the MMC simulations. Simulated atom−atom distances converged to the EXAFS-derived distances within 10⁶ cycles.

The alloy cluster of 4.4 nm diameter was generated as described above, with the exception that the fcc Pt cluster was

first generated with the EXAFS-derived unit cell parameters (deduced from the measured interatomic distances) in a 4.4 nm cubic box and randomly replaced by Ru atoms with a probability of 0.5 using the DISCUS CHEM function.[36] The alloy cluster was further distorted as described above with the EXAFS-measured metal−metal distances of $d_{Pt-Pt} = 2.740$ Å, $d_{Pt-Ru} = 2.718$ Å, and $d_{Ru-Ru} = 2.690$ Å and the distortions of $\gamma_{Pt} = \gamma_{Ru} = 0.005$ Å.

The powder diffraction data were simulated using the "powder" subroutine with built-in "Debye" function in DISCUS.[36] The coordination numbers for the first through fourth coordination shells for Pt in the model core−shell clusters were calculated using the "CHEM" subroutine in the DISCUS package and compared to the experimental results from the EXAFS analysis.

Supporting Information Available: Additional TEM and STEM analytical data, EXAFS data, PDF simulations and refinements. This material is available free of charge *via* the Internet at http://pubs.acs.org.

REFERENCES AND NOTES

1. Bratlie, K. M.; Lee, H.; Komvopoulos, K.; Yang, P. D.; Somorjai, G. A. Platinum Nanoparticle Shape Effects on Benzene Hydrogenation Selectivity. *Nano Lett.* **2007**, *7*, 3097–3101.
2. Xiong, Y. J.; McLellan, J. M.; Chen, J. Y.; Yin, Y. D.; Li, Z. Y.; Xia, Y. N. Kinetically Controlled Synthesis of Triangular and Hexagonal Nanoplates of Palladium and Their SPR/SERS Properties. *J. Am. Chem. Soc.* **2005**, *127*, 17118–17127.
3. Park, K. H.; Jang, K.; Kim, H. J.; Son, S. U. Near-Monodisperse Tetrahedral Rhodium Nanoparticles on Charcoal: The Shape-Dependent Catalytic Hydrogenation of Arenes. *Angew. Chem., Int. Ed.* **2007**, *46*, 1152–1155.
4. Zhou, S. H.; Varughese, B.; Eichhorn, B.; Jackson, G.; McIlwrath, K. Pt−Cu Core−Shell and Alloy Nanoparticles for Heterogeneous NOx Reduction: Anomalous Stability and Reactivity of a Core−Shell Nanostructure. *Angew. Chem., Int. Ed.* **2005**, *44*, 4539–4543.
5. Alayoglu, S.; Nilekar, A. U.; Mavrikakis, M.; Eichhorn, B. Ru−Pt Core−Shell Nanoparticles for Preferential Oxidation of Carbon Monoxide in Hydrogen. *Nat. Mater.* **2008**, *7*, 333–338.
6. Park, J. I.; Kim, M. G.; Jun, Y. W.; Lee, J. S.; Lee, W. R.; Cheon, J. Characterization of Superparamagnetic "Core−Shell" Nanoparticles and Monitoring Their Anisotropic Phase Transition to Ferromagnetic "Solid Solution" Nanoalloys. *J. Am. Chem. Soc.* **2004**, *126*, 9072–9078.
7. Chou, N. H.; Schaak, R. E. Shape-Controlled Conversion of β-Sn Nanocrystals into Intermetallic M−Sn (M = Fe, Co, Ni, Pd) Nanocrystals. *J. Am. Chem. Soc.* **2007**, *129*, 7339–7345.
8. Ha, T. H.; Koo, H. J.; Chung, B. H. Shape-Controlled Syntheses of Gold Nanoprisms and Nanorods Influenced by Specific Adsorption of Halide Ions. *J. Phys. Chem. C* **2007**, *111*, 1123–1130.
9. Habas, S. E.; Lee, H.; Radmilovic, V.; Somorjai, G. A.; Yang, P. Shaping Binary Metal Nanocrystals through Epitaxial Seeded Growth. *Nat. Mater.* **2007**, *6*, 692–697.
10. Fan, F. R.; Liu, D. Y.; Wu, Y. F.; Duan, S.; Xie, Z. X.; Jiang, Z. Y.; Tian, Z. Q. Epitaxial Growth of Heterogeneous Metal Nanocrystals: From Gold Nano-Octahedra to Palladium and Silver Nanocubes. *J. Am. Chem. Soc.* **2008**, *130*, 6949.
11. Garcia-Gutierrez, D.; Gutierrez-Wing, C.; Miki-Yoshida, M.; Jose-Yacaman, M. HAADF Study of Au−Pt Core−Shell Bimetallic Nanoparticles. *Appl. Phys. A* **2004**, *79*, 481–487.
12. Liu, H. B.; Pal, U.; Medina, A.; Maldonado, C.; Ascencio, J. A. Structural Incoherency and Structure Reversal in Bimetallic Au−Pd Nanoclusters. *Phys. Rev. B* **2005**, *71*, 075403.
13. Chen, Y. M.; Yang, F.; Dai, Y.; Wang, W. Q.; Chen, S. L. Ni@Pt Core−Shell Nanoparticles: Synthesis, Structural and Electrochemical Properties. *J. Phys. Chem. C* **2008**, *112*, 1645–1649.
14. Siepen, K.; Bonnemann, H.; Brijoux, W.; Rothe, J.; Hormes, J. EXAFS/XANES, Chemisorption and IR Investigations of Colloidal Pt/Rh Bimetallic Catalysts. *Appl. Organomet. Chem.* **2000**, *14*, 549–556.
15. Nashner, M. S.; Frenkel, A. I.; Somerville, D.; Hills, C. W.; Shapley, J. R.; Nuzzo, R. G. Core Shell Inversion during Nucleation and Growth of Bimetallic Pt/Ru Nanoparticles. *J. Am. Chem. Soc.* **1998**, *120*, 8093–8101.
16. Hills, C. W.; Nashner, M. S.; Frenkel, A. I.; Shapley, J. R.; Nuzzo, R. G. Carbon Support Effects on Bimetallic Pt−Ru Nanoparticles Formed from Molecular Precursors. *Langmuir* **1999**, *15*, 690–700.
17. Nashner, M. S.; Frenkel, A. I.; Adler, D. L.; Shapley, J. R.; Nuzzo, R. G. Structural Characterization of Carbon-Supported Platinum−Ruthenium Nanoparticles from the Molecular Cluster Precursor $PtRu_5C(CO)_{16}$. *J. Am. Chem. Soc.* **1997**, *119*, 7760–7771.
18. Long, J. W.; Stroud, R. M.; Swider-Lyons, K. E.; Rolison, D. R. How to Make Electrocatalysts more Active for Direct Methanol Oxidation—Avoid PtRu Bimetallic Alloys! *J. Phys. Chem. B* **2000**, *104*, 9772–9776.
19. Hammer, B.; Morikawa, Y.; Norskov, J. K. CO Chemisorption at Metal Surfaces and Overlayers. *Phys. Rev. Lett.* **1996**, *76*, 2141–2144.
20. Lewera, A.; Zhou, W. P.; Vericat, C.; Chung, J. H.; Haasch, R.; Wieckowski, A.; Bagus, P. S. XPS and Reactivity Study of Bimetallic Nanoparticles Containing Ru and Pt Supported on a Gold Disk. *Electrochim. Acta* **2006**, *51*, 3950–3956.
21. Holmblad, P. M.; Larsen, J. H.; Chorkendorff, I.; Nielsen, L. P.; Besenbacher, F.; Stensgaard, I.; Laegsgaard, E.; Kratzer, P.; Hammer, B.; Norskov, J. K. Designing Surface Alloys with Specific Active Sites. *Catal. Lett.* **1996**, *40*, 131–135.
22. Besenbacher, F.; Chorkendorff, I.; Clausen, B. S.; Hammer, B.; Molenbroek, A. M.; Norskov, J. K.; Stensgaard, I. Design of a Surface Alloy Catalyst for Steam Reforming. *Science* **1998**, *279*, 1913–1915.
23. Sasaki, K.; Mo, Y.; Wang, J. X.; Balasubramanian, M.; Uribe, F.; McBreen, J.; Adzic, R. R. Pt Submonolayers on Metal Nanoparticles—Novel Electrocatalysts for H_2 Oxidation and O_2 Reduction. *Electrochim. Acta* **2003**, *48*, 3841–3849.
24. Aiken, J. D.; Finke, R. G. A Review of Modern Transition-Metal Nanoclusters: Their Synthesis, Characterization, and Applications in Catalysis. *J. Mol. Catal. A* **1999**, *145*, 1–44.
25. Martin, T. P.; Bergmann, T.; Gohlich, H.; Lange, T. Shell Structure of Clusters. *J. Phys. Chem.* **1991**, *95*, 6421–6429.
26. Schmid, G. Large Clusters and Colloids—Metals in the Embryonic State. *Chem. Rev.* **1992**, *92*, 1709–1727.
27. Schmid, G. Chemical Synthesis of Large Metal Clusters and Their Properties. *Nanostruct. Mater.* **1995**, *6*, 15–24.
28. Alayoglu, S.; Eichhorn, B. Rh−Pt Bimetallic Catalysts: Synthesis, Characterization, and Catalysis of Core−Shell, Alloy, and Monometallic Nanoparticles. *J. Am. Chem. Soc.* **2008**, *130*, 17479–17486.
29. Park, J. Y.; Zhang, Y.; Grass, M.; Zhang, T.; Somorjai, G. A. Tuning of Catalytic CO Oxidation by Changing Composition of Rh−Pt Bimetallic Nanoparticles. *Nano Lett.* **2008**, *8*, 673–677.

30. Toby, B. H. EXPGUI, a Graphical User Interface for GSAS. *J. Appl. Crystallogr.* **2001**, *34*, 210–213.

31. Chupas, P. J.; Chapman, K. W.; Lee, P. L. Applications of an Amorphous Silicon-Based Area Detector for High-Resolution, High-Sensitivity and Fast Time-Resolved Pair Distribution Function Measurements. *J. Appl. Crystallogr.* **2007**, *40*, 463–470.

32. Chupas, P. J.; Qiu, X. Y.; Hanson, J. C.; Lee, P. L.; Grey, C. P.; Billinge, S. J. L. Rapid-Acquisition Pair Distribution Function (RA-PDF) Analysis. *J. Appl. Crystallogr.* **2003**, *36*, 1342–1347.

33. Hahn, T. *International Tables for Crystallography*, 2nd ed.; Kluwer Academic Publishers: Dordrecht, The Netherlands, **1989**; Vol. A.

34. Ravel, B.; Newville, M. ATHENA, ARTEMIS, HEPHAESTUS: Data Analysis for X-ray Absorption Spectroscopy Using IFEFFIT. *J. Synchrotron Radiat.* **2005**, *12*, 537–541.

35. Zabinsky, S. I.; Rehr, J. J.; Ankudinov, A.; Albers, R. C.; Eller, M. J. Multiple-Scattering Calculations of X-ray-Absorption Spectra. *Phys. Rev. B* **1995**, *52*, 2995–3009.

36. Proffen, T.; Neder, R. B. DISCUS: A Program for Diffuse Scattering and Defect-Structure Simulation. *J. Appl. Crystallogr.* **1997**, *30*, 171–175.

37. Via, G. H.; Drake, K. F.; Meitzner, G.; Lytle, F. W.; Sinfelt, J. H. Analysis Of EXAFS Data on Bimetallic Clusters. *Catal. Lett.* **1990**, *5*, 25–33.

38. Wang, Y.; Toshima, N. Preparation of Pd−Pt Bimetallic Colloids with Controllable Core/Shell Structures. *J. Phys. Chem. B* **1997**, *101*, 5301–5306.

39. Page, K.; Proffen, T.; Terrones, H.; Terrones, M.; Lee, L.; Yang, Y.; Stemmer, S.; Seshadri, R.; Cheetham, A. K. Direct Observation of the Structure of Gold Nanoparticles by Total Scattering Powder Neutron Diffraction. *Chem. Phys. Lett.* **2004**, *393*, 385–388.

40. Bedford, N.; Dablemont, C.; Viau, G.; Chupas, P.; Petkov, V. 3-D Structure of Nanosized Catalysts by High-Energy X-ray Diffraction and Reverse Monte Carlo Simulations: Study of Ru. *J. Phys. Chem. C* **2007**, *111*, 18214–18219.

41. Hwang, B. J.; Sarma, L. S.; Chen, J. M.; Chen, C. H.; Shih, S. C.; Wang, G. R.; Liu, D. G.; Lee, J. F.; Tang, M. T. Structural Models and Atomic Distribution of Bimetallic Nanoparticles as Investigated by X-ray Absorption Spectroscopy. *J. Am. Chem. Soc.* **2005**, *127*, 11140–11145.

42. Hwang, B. J.; Sarma, L. S.; Chen, C. H.; Bock, C.; Lai, F. J.; Chang, S. H.; Yen, S. C.; Liu, D. G.; Sheu, H. S.; Lee, J. F. Controlled Synthesis and Characterization of Ru-Core−Pt-Shell Bimetallic Nanoparticles. *J. Phys. Chem. C* **2008**, *112*, 19922–19929.

43. Farrow, C. L.; Juhas, P.; Liu, J. W.; Bryndin, D.; Bozin, E. S.; Bloch, J.; Proffen, T.; Billinge, S. J. L. PDFfit2 and PDFgui: Computer Programs for Studying Nanostructure in Crystals. *J. Phys.: Condens. Matter* **2007**, *19*, 335219.

44. Korsunskiy, V. I.; Neder, R. B. Exact Model Calculations of the Total Radial Distribution Functions for the X-ray Diffraction Case and Systems of Complicated Chemical Composition. *J. Appl. Crystallogr.* **2005**, *38*, 1020–1027.

45. Mavrikakis, M.; Hammer, B.; Norskov, J. K. Effect of Strain on the Reactivity of Metal Surfaces. *Phys. Rev. Lett.* **1998**, *81*, 2819–2822.

46. Hammer, B.; Norskov, J. K. Electronic Factors Determining the Reactivity of Metal Surfaces. *Surf. Sci.* **1995**, *343*, 211–220.

47. Schlapka, A.; Lischka, M.; Gross, A.; Kasberger, U.; Jakob, P. Surface Strain *versus* Substrate Interaction in Heteroepitaxial Metal Layers: Pt on Ru(0001). *Phys. Rev. Lett.* **2003**, *91*, 016101.

48. Ortigoza, M. A.; Stolbov, S.; Rahman, T. S. Formation of Pt Islets on Facets of Ru Nanoparticles: First-Principles Study. *Phys. Rev. B* **2008**, *78*, 195417.

49. Hoster, H. E.; Bergbreiter, A.; Erne, P. M.; Hager, T.; Rauscher, H.; Behm, R. J. $Pt_xRu_{1−x}$/Ru(0001) Surface Alloys—Formation and Atom Distribution. *Phys. Chem. Chem. Phys.* **2008**, *10*, 3812–3823.